
This is an electronic reprint of the original article.
This reprint may differ from the original in pagination and typographic detail.

Calle Gonzales, Miguel; Oshiro, Roberto E.; Körgesaar, Mihkel; Alves, Marcílio; Kujala, Pentti
Combined strain rate, mesh size and calibration test influence on structural failure: Miniature ship grounding test

Published in:
Ocean Engineering

DOI:
[10.1016/j.oceaneng.2019.01.002](https://doi.org/10.1016/j.oceaneng.2019.01.002)

Published: 01/02/2019

Document Version
Peer-reviewed accepted author manuscript, also known as Final accepted manuscript or Post-print

Published under the following license:
CC BY-NC-ND

Please cite the original version:
Calle Gonzales, M., Oshiro, R. E., Körgesaar, M., Alves, M., & Kujala, P. (2019). Combined strain rate, mesh size and calibration test influence on structural failure: Miniature ship grounding test. *Ocean Engineering*, 173, 215-226. <https://doi.org/10.1016/j.oceaneng.2019.01.002>

This material is protected by copyright and other intellectual property rights, and duplication or sale of all or part of any of the repository collections is not permitted, except that material may be duplicated by you for your research use or educational purposes in electronic or print form. You must obtain permission for any other use. Electronic or print copies may not be offered, whether for sale or otherwise to anyone who is not an authorised user.

1 Combined strain rate, mesh size and calibration test influence on 2 structural failure: miniature ship grounding test

3

4 Miguel A. G. Calle*[†], Roberto E. Oshiro**, Mihkel Kõrgesaar***, Marcilio Alves**, Pentti Kujala*

5 * Marine Technology Research Group, Department of Mechanical Engineering, Aalto University, Tietotie 1C,
6 Espoo, Finland

7 ** Group of Solid Mechanics and Impact Structure, Department of Mechatronics and Mechanical Systems,
8 Polytechnic School of the University of Sao Paulo, Av. Prof. Mello Moraes 2231, Sao Paulo, SP, Brazil

9 *** Tallinn University of Technology, School of Maritime Academy, Tallinna 19, Kuressaare, Estonia

10 [†] corresponding author: mcallegonzales@gmail.com, miguel.calle@aalto.fi

11

12 Abstract

13 This paper investigates the influence of the strain rate and element size on the fracture of steel plates
14 presented in marine structures undergoing grounding when modeled by the finite element method. Three
15 different experimental tests (tensile, tearing and perforation tests), performed at different velocities, are used
16 in the study. These tests are conceived to cover diverse rupture modes related mainly to crack initiation and
17 propagation. Plastic strain- and stress state-based failure criteria were calibrated from these experiments.
18 Sensitivity to strain rate and mesh size were also evaluated. A ship grounding event was reproduced
19 experimentally in 1:100 reduced scale. This experiment was FE modeled to evaluate the performance of the
20 aforementioned failure criteria. The results verified the significant influence of the strain rate and stress state
21 on the failure strain. In addition, it is shown that the sole use of tensile tests is not enough to properly
22 characterize the material failure observed in the structural collapse mode of the miniature ship bottom
23 structure. This collapse is shown to be a combination of stretching and tearing of structural members.

24

25 **keywords:** material failure, strain rate sensitivity, tensile tests, tearing tests, perforation tests

1 **1. Introduction**

2 During the last decades, several researchers investigated collision accidents of marine structures using
3 numerical methods. The finite element method showed to be one of the most reliable tools to predict the
4 acting forces and damaged configuration of marine structures when subjected to collision/grounding tests.

5 In the last few years, the rapid increase of computational processing power allowed the consideration of
6 diverse non-linearities so that the output results became more and more accurate. Clearly, it is valuable to
7 discern what aspects are more or less relevant in an analysis so one can retrieve accurate output results.

8 Among the main aspects that affects the accuracy of a FE analysis one can list:

- 9 • Shell elements: In view of the huge dimensions of marine structures when compared to the plate
10 thickness used in shipbuilding, the use of shell elements became mandatory to reduce the number of
11 elements so avoiding long computational times. This is true despite of the fact that shell elements
12 incorporate rotational degrees of freedom and local systems, which are computationally difficult to
13 parametrize/update, and are inadequate to model large longitudinal and transverse shear strains
14 (Flores, 2016). Even so, shell finite elements are still considered as the standard element to model
15 marine structures subjected to collision (Calle and Alves, 2015; Liu et al., 2018).
- 16 • Strain rate sensitivity on flow stress: Taken into account the dynamic character of ship
17 collision/grounding events, the strain rate sensitivity on flow stress of shipbuilding steels is being
18 included in recent numerical-experimental works when material undergoes plastic deformation at
19 high loading rates (Choung et al., 2010; Choung et al., 2013; Storheim and Amdahl, 2017; Paik et al.,
20 2017). To do it, some well-known constitutive material models, such as Cowper-Symonds (1957) and
21 Johnson-Cook (1985), are being used so making evident the strong influence of the strain rate on the
22 plastic hardening of steels.
- 23 • Material fracture: It is widely known that the definition of the parameters of the failure criteria is the
24 most important key point for a correct prediction of a realistic structural collapse mode and an
25 acceptable quantification of the impact energy absorption in the FE modeling of ship collision and
26 grounding events (Calle and Alves, 2015). The equivalent plastic failure strain is the most common

1 material fracture criterion employed in the analyses of ship collision and grounding events. In this
2 work, the equivalent plastic strain at failure is also denoted “failure strain” as widely termed by diverse
3 works in marine engineering (Ehlers and Varsta, 2009; Choung et al., 2012; Storheim et al., 2015;
4 Marinatos and Samuelides, 2015). The failure strain is usually evaluated experimentally via uniaxial
5 tensile tests. However, this value depends on many factors and exhibits a scatter as large as 10% to
6 70%, according to the literature review made by Calle and Alves (2015). For instance, early works on
7 FE modeling of ship collision already considered the numerical influence of the shell element size on
8 the failure strain according to Barba’s law. So, uniaxial tensile tests needed to be FE modeled at
9 different element sizes to calibrate the failure strain (Peschmann and Kulzep, 2000; Yamada et al.,
10 2005; Ehlers, 2010; Hogström, 2012). However, some other physical factors are more difficult to be
11 considered into the material failure criteria as commented below.

- 12 • Strain rate sensitivity on material fracture: this is a challenging aspect to be considered and
13 implemented in FE codes and in failure criteria (Paik, 2007a; Kim et al., 2016; Paik et al., 2017, Storheim
14 and Amdahl, 2017). Jones (1989) proposed an inverse form of the Cowper-Symonds formulation that
15 reproduces the experimental decrease observed in the failure strain when strain rate rises (Paik and
16 Pedersen, 1996; Yamada et al., 2005; Paik, 2007b). However, the parameters for this inverse
17 formulation differ to that for the traditional Cowper-Symonds formulation for mild steels ($C = 40.4 \text{ s}^{-1}$, $p = 5$) (Paik and Thayamballi, 2003; Paik, 2007a; Paik, 2007b) so requiring, anyway, a particular
18 mechanical characterization procedure. The influence of the strain rate on the material fracture varies
19 from one material to another (Paik et al., 2017) and, depending on the analyzed strain rate range, also
20 requires the consideration of temperature effects by the model (Roth and Mohr, 2014). Additionally,
21 it is not completely clear how the strain rate influences the structural response of large marine
22 structures subjected to collision. For these reasons, most of the researches assume low structural
23 influence of strain rate on material fracture during ship collision events or, basically, assume a lower
24 equivalent plastic strain at failure due to dynamic influence (Endo et al., 2002; Yagi et al., 2009;
25 AbuBakar and Dow, 2013; Bela et al., 2017; Farinha et al., 2018; among others).

- 1 • Crack propagation: FE modeling of material fracture is further complicated when it is induced by crack
2 propagation. Most of the material fracture criteria are conceived for FE modeling of the crack initiation
3 process, so they work accurately when modeling the first element removal. After that, the crack shape
4 remains unrealistic and unrealistic levels of energy to propagate it are obtained. This leads to modeling
5 errors (Calle and Alves, 2015). Uniaxial tensile tests are widely used for mechanical characterization
6 of the materials including fracture evaluation. In this kind of test, the crack initiation process prevails
7 in the rupture process once the crack is generated in the middle section of the sample and the
8 complete rupture given by the propagation of the crack is abrupt. Thus, some authors perform
9 experimental and numerical studies focused on crack propagation (Simonsen and Törnqvist, 2004;
10 Kõrgesaar and Romanoff, 2013). As a result, Simonsen and Törnqvist (2004) obtained an increase of
11 40% in the equivalent strain at failure when compared to that calibrated by tensile test. However, so
12 far, no unified approach to cover both initiation and propagation of fracture exists.
- 13 • Stress state on material fracture: material failure criteria based on the equivalent plastic strain (failure
14 strain criteria) are inaccurate when the FE modeled structure is subjected to stress states different of
15 the one presented in uniaxial tensile tests, e.g. biaxial tension or shear loadings. Some authors justified
16 the use of a failure strain criterion by the low variation of triaxialities in fracture during a ship
17 collision/grounding event or by making use of an average plastic strain value to include both crack
18 initiation and propagation phenomena (Calle et al., 2017a). Some authors developed material failure
19 criteria to model collision of marine structures that includes the stress states into its formulations
20 (Lehmann and Yu, 1998; Kitamura and Endo, 2000; Törnqvist, 2003; Kõrgesaar and Romanoff, 2014;
21 Kõrgesaar, 2019) so obtaining accurate modeling results.

22 Together with these aspects, it is worth mentioning that ship grounding is a complex event in which the major
23 part of energy dissipation occurs in inelastic straining (Nguyen et al., 2012). Two possible scenarios of ship
24 grounding can be considered (Paik and Thayamballi, 2003): the first, called properly “grounding” or “powered
25 grounding”, results in a raking damage of the ship bottom structure induced by a horizontal slide over a seabed
26 obstacle. The second, called “stranding”, takes place when the ship bottom structure at standstill is vertically

1 pressed by an obstacle due to pitch and/or heave ship movements. In general, real grounding accidents
2 combine these two scenarios, with penetration and tearing of the ship bottom structure. As a consequence,
3 structural members are subjected mainly to lateral-edge (tearing or cutting) and in-plane (membrane) forces,
4 so inducing high and low levels of energy dissipation respectively. According to Nguyen et al. (2011), this
5 energy dissipation is the key aspect for modeling. Besides, the contour geometry of seabed obstacles (rock,
6 reef or shoal) can also affect this energy dissipation. On the one hand, rock obstacles easily perforate outer
7 plates so inducing local damages; on the other hand, large shoal obstacles may deform larger parts of the
8 bottom structure (Alsos and Amdahl, 2007).

9 Having in mind this scenario, this paper presents an experimental investigation about the influence of strain
10 rate on the material fracture of a mild steel plate aiming the finite element modeling of a ship-grounding
11 event. A miniature ship grounding experiment was also performed to validate the numerical results. Three
12 different mechanical tests (uniaxial tensile, perforation and out-of-plane tearing) are used to calibrate the
13 failure strain at different strain rates, intended to recreate different rupturing modes observed in ship collision
14 and grounding, particularly that related to crack initiation (tensile and perforation) and propagation (tearing).

15 **2. Base material strain hardening**

16 **2.1 Material and experiments**

17 Uniaxial tensile tests were performed in a cold-rolled SAE 1008 carbon steel sheet with 0.25 mm thickness
18 subjected to quasi-static and dynamic conditions.

19 In order to evaluate the mechanical behavior in quasi-static conditions, standard dog-bone specimens were
20 subjected to uniaxial tensile test. The dimensions of the reduced section of the specimen are 50 mm length ×
21 10 mm width. The test velocity was set in 0.0025 mm/s so inducing an average strain rate of $4.1 \times 10^{-5} \text{ s}^{-1}$.

22 The strain data was acquired by Digital Image Correlation (DIC) technique employing a virtual mesh on the
23 sample surface with uniform 0.5 mm side square elements. A maximum plastic strain at failure of 0.5822 was
24 measured in the middle of the ruptured specimen section at a strain rate of $3.8 \times 10^{-4} \text{ s}^{-1}$.

25 Given that the mechanical strength of carbon steels increases at higher strain rates, small dog-bone specimens
26 were subjected to uniaxial tensile tests to evaluate the strain rate sensitivity of the material. Tensile tests at

1 different test velocities were performed in an earlier work (Calle et al., 2017b) using small tensile specimens
 2 based on a Hopkinson bar machine tensile samples designed by Verleysen et al. (2008). The dimensions of the
 3 reduced section of the small specimen are 5 mm length \times 4 mm width, and the distance between the sample
 4 shoulders is 9 mm.

5 For all tensile tests, the true stress-strain curves are obtained from engineering stress-strain curves. At the
 6 same time, the engineering stress-strain curves are obtained from the force-displacement responses of the
 7 tensile test experiments as follows:

$$8 \quad \sigma = (1 + e) S \quad (1)$$

$$9 \quad \varepsilon = \ln(1 + e) \quad (2)$$

$$10 \quad S = F/A_0 \quad (3)$$

$$11 \quad e = \delta/L_0 \quad (4)$$

12 where σ and ε are the true stress and true strain respectively, S and e are the engineering stress and
 13 engineering strain respectively, F and δ are the force and displacement acquired from the testing machine,
 14 L_0 and A_0 are the initial length and area of the tensile samples.

15 The instantaneous strain rate is defined as the rate at which the strain occurs and is given by

$$16 \quad \dot{\varepsilon} = d\varepsilon/dt \quad (5)$$

17 Particularly for the analysis of the increment of the true stress level at dynamic conditions, Eq. (12), an average
 18 strain rate is considered by averaging the strain rates in between yield point and below the necking point as

$$19 \quad \bar{\varepsilon} = \frac{1}{\Delta t} \int \dot{\varepsilon} dt \quad (6)$$

20 **2.2 Strain rate-dependent plasticity model**

21 The material is assumed as isotropic and the elasto-plastic constitutive law follows the J_2 -flow theory, i.e., the
 22 Von Mises yield surface with isotropic hardening and associated flow rule as

$$23 \quad \Theta(\bar{\sigma}, \sigma_f) = \bar{\sigma} - \sigma_f(\varepsilon, \dot{\varepsilon}) = 0 \quad (7)$$

$$24 \quad \bar{\sigma} = \sqrt{3J_2} \quad (8)$$

$$25 \quad J_2 = \frac{1}{6}[(\sigma_1 - \sigma_2)^2 + (\sigma_2 - \sigma_3)^2 + (\sigma_3 - \sigma_1)^2] \quad (9)$$

1 where $\bar{\sigma}$ is the Von Mises equivalent stress, the flow stress $\sigma_f(\varepsilon, \dot{\varepsilon})$ is assumed as a function of the equivalent
2 plastic strain ε and the equivalent plastic strain rate $\dot{\varepsilon}$.

3 The increment of equivalent plastic strain is given as a function of the principal strain components as

$$4 \quad d\varepsilon = \sqrt{\frac{2}{3} [d\varepsilon_1^2 + d\varepsilon_2^2 + d\varepsilon_3^2]} \quad (10)$$

5 A power law constitutive model to reproduce the true stress strain behavior of the material, at quasi-static
6 loading conditions, is given as follows

$$7 \quad \sigma_0 = \begin{cases} \sigma_y & \varepsilon \leq \varepsilon_L \\ K\varepsilon^n & \varepsilon > \varepsilon_L \end{cases} \quad (11)$$

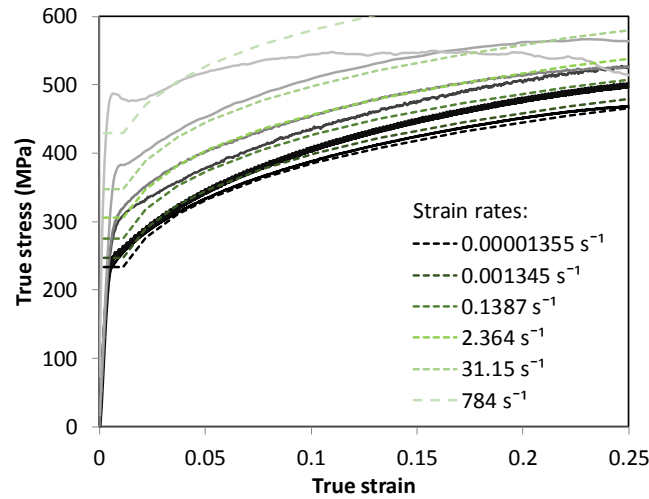
8 where σ_0 is the true stress at quasi-static conditions, ε is the equivalent plastic strain, σ_y is the yield stress, K
9 and n are the material parameters and $\varepsilon_L = (\sigma_y/K)^{1/n}$ to ensure curve continuity. Parameters K and n are
10 adjusted using a log-log approach, considering the points above the yield point and region below the necking
11 point, and listed in Table 1.

12 The increment on the true stress levels due to the increment on the strain rate is widely evaluated at a
13 reference plastic strain value commonly set between 5% and 20%. Notwithstanding, in several cases, it results
14 in a poor fitting at higher strain rates due to the gradual material thermal softening. Thermal softening occurs
15 by the adiabatic heating of the material when strained at high velocities (Mason et al., 1994; Kapoor and
16 Nemat-Nasser, 1998).

17 Aiming at a better fit, even at high strain rates, the strain rate sensitivity constitutive model given by Alves
18 (2000) was adopted to introduce the strain rate sensitivity to the flow stress as follows

$$19 \quad \sigma_f = \sigma_0 + \sigma_y \left(\frac{\dot{\varepsilon}}{C} \right)^{1/p} \quad (12)$$

20 where σ_f is the flow stress (or true stress at dynamic/general conditions), σ_0 is true stress at quasi-static
21 conditions, Eq. (11), σ_y is the yield stress, $\dot{\varepsilon}$ is the equivalent strain rate, C and p are material parameters
22 obtained by data log-log fitting. The material parameters, obtained at 10% plastic strain, are presented in
23 Table 1.



1

2

Fig. 1. Experimental and fitted true stress-strain curves at different strain rates.

3

Table 1. Material parameters.

σ_y	226.9 MPa
K	626.9 MPa
n	0.2077
C	1346.9 s ⁻¹
p	6.4671

4

Next, this material model was implemented in the commercial code Abaqus/CAE 2016 – explicit analysis. Shell

5

elements (homogeneous type) with five integration points are considered in all FE models. The coupled Power

6

law plus Alves model (Eq. 12) is used to describe the plastic strain hardening and strain rate sensitivity by

7

listing the “yield stress” as a function of the “plastic strain” and “rate” (strain rate). The failure strain is

8

modeled by using the “ductile damage” parameter. To reduce the processing time, “semi-automatic mass

9

scaling” technique is used in the numerical modeling of all mechanical tests.

10

3. Base material failure

11

3.1 Experiments on uniaxial tensile loading

12

Failure strain for plate metals are commonly obtained using standard uniaxial tensile specimens. However,

13

the long length of standard dog-bone specimens does not allow achieving high strain rates (Verleysen et al.,

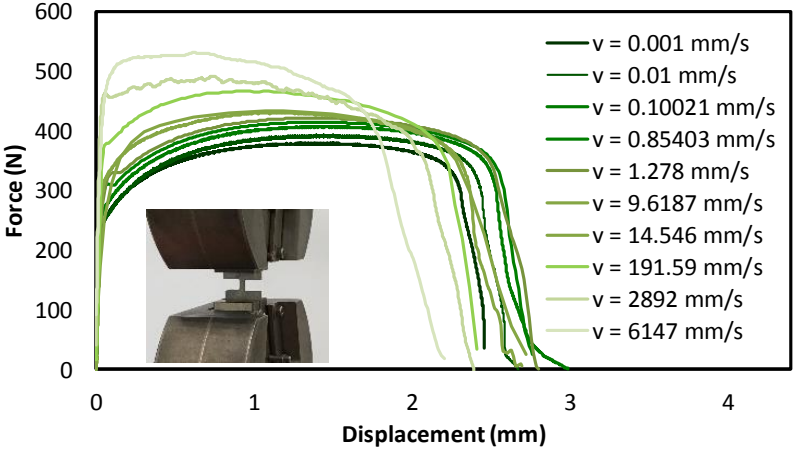
14

2008). Tensile tests in small specimens (section 2) are performed here to calibrate the strains at failure.

1 The tensile tests in small specimens are FE modeled to reproduce the material rupture at different test
2 velocities. Uniform 0.5×0.5 mm shell elements are considered for the FE model. An iterative calibration
3 procedure was performed in order to equate numerical and experimental elongation-to-rupture responses at
4 each test velocity.

5 Given the relatively large element size used in the FE modeling of small specimens when compared with the
6 specimen dimension, the after necking force response in the tensile test become infeasible to be FE modeled
7 accurately. Moreover, at higher test velocities, numerical and experimental force-elongation curves diverge
8 moderately at large plastic strains because of the material softening, as commented previously in section 2.
9 For these reasons, material failure was calibrated using as a reference the equivalence in absorbed energy
10 before material fracture, i.e., the area under the force-displacement curves.

11 The influence of mesh size on the failure strain is evaluated with the quasi-static tensile test with standard
12 dog-bone specimen (section 2). This test was FE modeled considering different mesh sizes with ratios of
13 equivalent length over thickness (L_e/t) in a range from 2.0 to 20 (0.5×0.5 , 0.625×0.625 , 1.0×1.0 , $1.667 \times$
14 1.667 , 2.5×2.5 , 5×3.333 and 5×5 mm). These models are presented in Appendix A.1. For rectangular-shaped
15 shell elements with dimensions $L_1 \times L_2$, the equivalent length is defined as $L_e = \sqrt{L_1 \cdot L_2}$. An elongation at
16 rupture of 18.3 mm was set as a common reference to calibrate the failure strains for different mesh sizes. It
17 corresponds to the elongation at rupture obtained numerically considering 0.5822 failure strain as
18 experimentally measured using DIC technique.



19

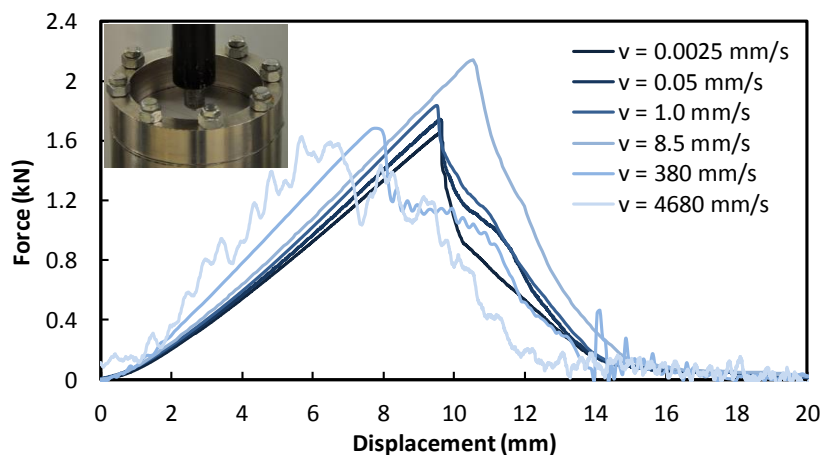
1 Fig. 2. Experiment setup and force responses obtained from uniaxial tensile tests in small specimen at
2 different velocities.

3 3.2 Experiments on perforation loading

4 Perforation tests in $\varnothing 80$ mm circular plates were conducted at different indentation velocities. Circular
5 specimens were peripherally clamped in a cylindrical holed support using clamps with serrated surfaces in
6 order to prevent sliding of the plate boundaries. A rigid cylindrical indenter with 90° cone head spherically
7 smoothed by a 3.4 mm radius was used.

8 The perforation tests were performed in three different experimental setups: universal screw-driven test
9 machine, all-electric dynamic testing machine and a low-energy drop weight machine. In the drop weight
10 machine, a falling mass of 0.76 kg was used and its velocity, $\dot{u}(t)$, was acquired by a laser Doppler vibrometer.
11 Then, the mass displacement and acceleration were obtained by integrating and deriving the velocity signal
12 such as $u = \int \dot{u}(t) dt$ and $\ddot{u} = d\dot{u}(t)/dt$ respectively and the force by multiplying acceleration by the falling
13 mass, $F(t) = m \ddot{u}(t)$.

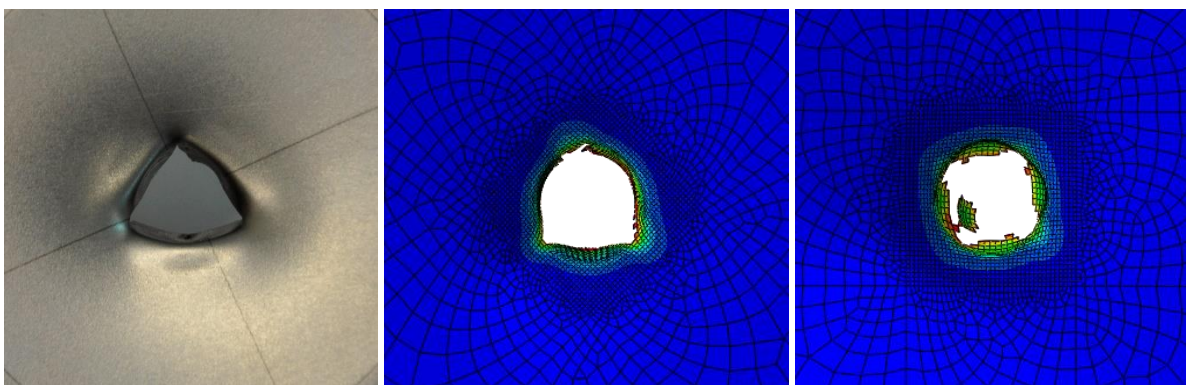
14 Fig. 3 shows the force-displacement responses obtained in the perforation tests. Higher force slopes are
15 observed at higher test velocities. In contrast, force peaks came down when the test speed was increased.
16 Moreover, diverse structural responses are observed after force peak is achieved.



17
18 Fig. 3. Experiment setup and force responses obtained from perforation tests at different velocities.

19 In order to calibrate the plastic strain at failure in the perforation test, FE modeling of the perforation tests at
20 different velocities were performed using uniform 0.5×0.5 mm shell elements. Given that no slipping was

1 detected between the circular support and the plates in the experiments, the FE model of the circular plate
2 was fully constrained in its perimeter. The plastic strain at failure is iteratively calibrated so to obtain
3 numerically a maximum peak force equivalent to that obtained experimentally for each test velocity.
4 In order to evaluate the influence of the mesh size on the material failure when modeling a perforation test,
5 FE modeling of the perforation test using different mesh sizes of shell elements are performed. The perforation
6 test response at 0.0025 mm/s was used as reference, which resulted in a peak force of 1.65 kN. Shell element
7 sizes with equivalent length over thickness ratios (L_e/t) ranging from 2 to 20 (0.5×0.5 , 1×1 , 2×2 , $3.333 \times$
8 3.333 , 4×4 and 5×5 mm) were employed. The geometry of these models are shown in Appendix A.2.
9 Given the relevant influence of friction on the stress state and ductile fracture of punched plates (Wiśniewski
10 and Kotakowski, 2003; Lee et al., 2004), FE models of perforation tests considering friction coefficients
11 between 0.1 and 0.3 were developed. Independently of the test speed, all perforation experiments generated
12 a fracture in triangular pattern (projection of three cracks from the central area). When FE modeling the
13 perforation test using a mesh size of 0.5×0.5 mm, a friction coefficient of 0.1 also induces a triangular fracture
14 pattern, while larger friction values (0.2 and 0.3) generates square-like fracture patterns as shown in Fig. 4.
15 However, when using larger mesh sizes, this distinction in fracture pattern is no longer observed. Nevertheless,
16 the friction coefficient was set in 0.1 since it generates numerically the same collapse mode observed in
17 experiments. At the same time, coefficient of 0.1 is reasonable for dynamic friction (Soares and Garbatov,
18 2015) and considering polished surfaces of both indenter and plate.



19
20 Fig. 4. Fracture patterns obtained from perforation test: a) experiment and b) FE modeling considering
21 friction coefficients of 0.1 and 0.2.

3.3 Experiments on out-of-plane tearing loading

Tearing tests based on the third fracture mode were performed at different velocities. It consists in a crack opening test by separating two plate strips by applying forces in out-of-plane opposite directions as shown in Fig. 5 (Calle et al., 2017a). Similar to the tensile test, the specimen's strips are clamped to both testing machine grips. The vertical displacement of the upper grip will induce the crack opening/propagation along the specimen's body.

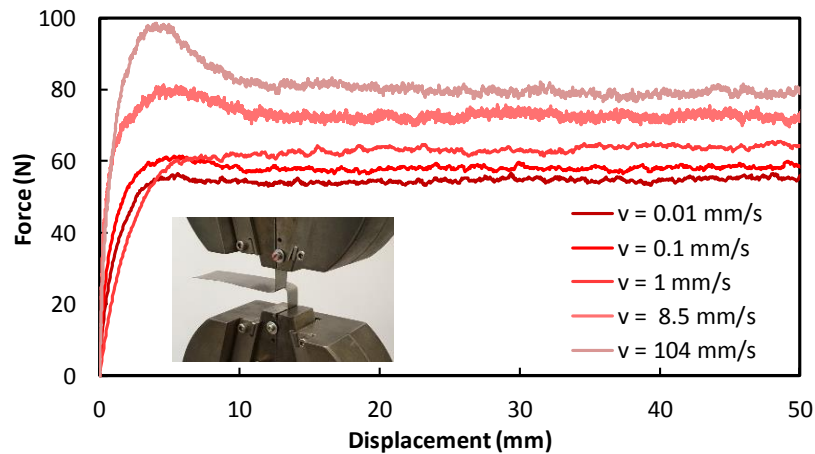


Fig. 5. Experiment setup and force responses obtained from tearing tests at different velocities.

For the tearing tests, two experimental setups were used: universal screw-driven and all-electric dynamic testing machines. Figure 5 presents the force-displacement responses for the tearing tests performed at several velocities. In a first stage, these strips are completely stretched in tension and a crack is generated. After that, the crack starts propagating showing a stable crack-opening force response. Some plate corrugation was detected besides the opened crack in all specimens. It is clearly observed that higher test velocities lead to higher tearing force-levels.

To evaluate the material failure strain at different tearing velocities a FE model was developed using uniform 0.5×0.5 mm shell elements and the coupled Power law plus Alves material model. An iterative process was performed to calibrate the plastic strains at failure in order to generate numerical equivalent force levels as the ones found in the experiments. This iterative procedure was repeated for each test velocity.

Mesh size influence on the failure strain was studied using different size shell elements. The crosshead velocity of 0.01 mm/s was used as reference for the test modeling so resulting in a nearly stable tearing force of 56.1

1 N. Different mesh sizes with equivalent length over thickness ratios (L_e/t) between 2 and 20 (0.5×0.5 , 1×1 ,
2 1.667×2 , 2.5×3.125 , 5×3.571 and 5×5 mm) were considered for the analysis. Some of these models are
3 presented in Appendix A.3.

4 Regardless of the mesh size, all FE models showed the same fracture pattern as obtained in the experiment,
5 i.e. straight crack propagation along the strip. Given the sudden removal of the failing shell elements along
6 the strip, high oscillations in the numerical force responses are generated. Larger shell element sizes lead to
7 high force oscillations during crack propagation.

8 **3.4 Stress triaxiality on failure**

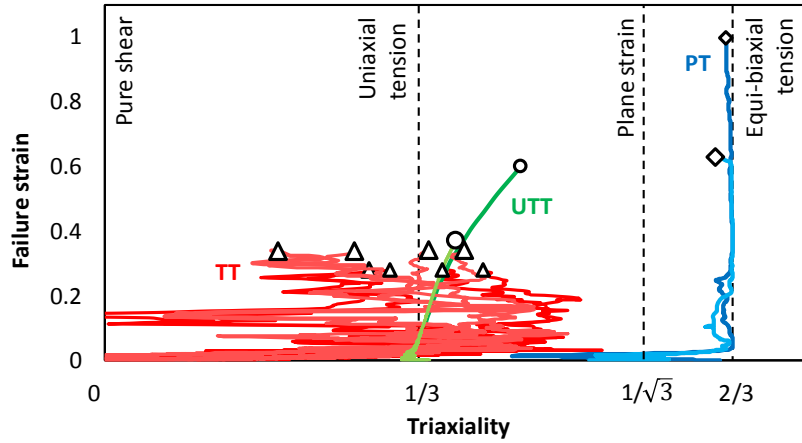
9 The evolution of the stress triaxiality for each one of the mechanical tests is presented in Fig. 6. Two ranges of
10 strain rates are considered. Markers indicate the failing points by uniaxial tensile \circ , perforation \diamond and tearing
11 Δ loadings. Small markers denote low strain rate and large markers high strain rate. Strain paths are built
12 considering the first integration point to fail (Fig. 6). However, in the case of the tearing tests, both outer-shell
13 integration points (1 & 5) are considered.

14 In the case of the uniaxial tensile tests in small specimens (UTT), the stress state was evaluated in the first
15 element to fail, i.e. the central element in the middle failure section of the specimen. Initially, the stress
16 triaxialities showed values close to $1/3$, then increasing up to values around 0.44. Regardless of the test
17 velocity, all strain paths present the same behavior, barely differing in the failure strain value. Larger strain
18 rates induce smaller failure strains.

19 For the perforation tests (PT), the stress state was also evaluated in the first element to fail, located in the
20 contact area between the spherical indenter and plate surface. In general, the stress triaxiality presented
21 steady values close to an equi-biaxial tension loading ($\eta = 2/3$) up to the rupture. Failure strains are significantly
22 higher than in uniaxial tensile tests. As seen in uniaxial tensile tests, higher strain rates induce lower failure
23 strains.

24 The stress state, observed in the tearing tests (TT), presented a different behavior when compared to the
25 other tests. The analysis was performed in failing elements along the propagated crack at low and high strain
26 rates. Unlike the other tests, strain path and failure occurrences vary according the integration points in the

1 same failing element. High stress triaxiality oscillations are observed in their strain paths. By contrast, larger
 2 strain rates induce larger failure strain, but in a smaller proportion.
 3 It is worth mentioning that the evaluation of stress states at failure is limited to the plane stress assumption
 4 of shell elements (so becoming unrealistic in case of triaxial loadings), and differs significantly from stress
 5 states evaluated in solid elements.



6
 7 Fig. 6. Failure strain versus triaxiality for all mechanical tests considering a mesh size of 0.5 mm ($L_e/t = 2$).

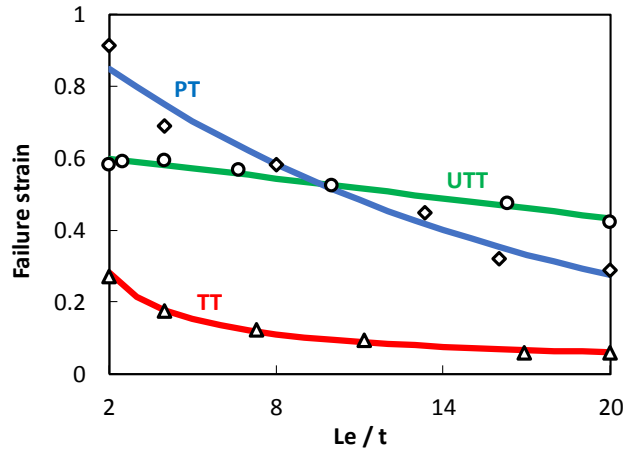
8 3.5 Influence of mesh size on failure

9 The influence of the mesh size on failure strain for each one of the three mechanical tests is shown in Fig. 7.
 10 This analysis comprises element sizes ranging from 0.5×0.5 mm to 5×5 mm (L_e/t ratios from 2 to 20
 11 respectively). Trend curves for the failure strain F_1 as a function of the L_e/t ratio are shown in Fig. 7 for each
 12 one of the mechanical tests. These curves do not have a particular form, they merely presented better data
 13 fitting. Normalized curves are also formulated as f_1 , considering a reference element length of $L_{e_0} = 0.5$ mm
 14 ($L_{e_0}/t = 2$), via

$$15 \quad f_1(L_e/t) = F_1(L_e/t)/F_1(L_{e_0}/t) \quad (13)$$

16 All tests showed strong sensitivity to mesh size. Uniaxial tensile test involves the uniform stretching of a
 17 material strip until the necking point and, from that point, the strain evolution is strongly dependent on the
 18 mesh size. In the perforation test, the plate failure is generated in circular areas of contact between the
 19 deformed plate surface and the rigid spherical indenter and these areas (and the induced strains) are sensitive
 20 to mesh size. In the tearing test, a crack is progressively opened and high plastic deformations and rupture of

1 the material occurs barely in a very small area near the crack tip. So, the induced plastic strains, close to the
 2 crack tip, are very sensitive to element size. When larger shell elements are used, the structural influence of
 3 the crack propagation in the whole shell area is diluted so yielding lower values of plastic strains at failure.



4
 5 Fig. 7. Dependence of failure strain on mesh size considering a mesh size of $L_e = 0.5$ mm ($L_e/t = 2$).

6 3.6 Influence of strain rate on failure

7 Figure 8a shows the influence of the strain rate on failure strain obtained from the uniaxial tensile, perforation
 8 and tearing tests. Given the dynamic character of this analysis, only mechanical tests that induces strain rates
 9 above 0.01 s^{-1} in the failing elements are taken into account. The strain rate values are computed as the
 10 instantaneous strain rates (Eq. 5) obtained from the first element to fail in each one of the mechanical tests
 11 (as also regarded in the analysis of stress triaxiality in failure, Fig. 6).

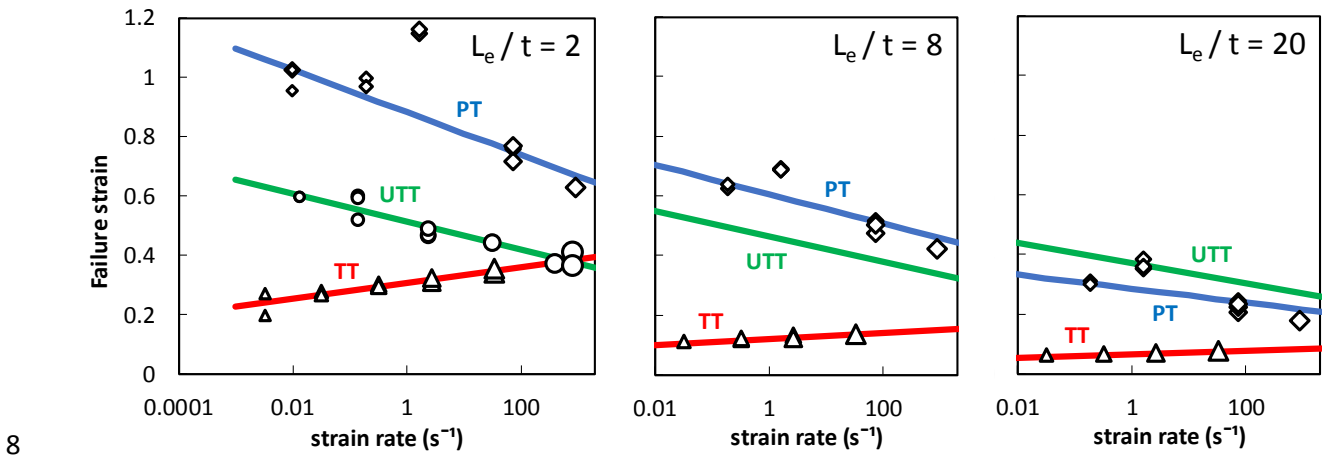
12 The failure strains for each one of the mechanical tests were numerically calibrated at different strain rates by
 13 FE modeling considering a uniform shell element size of 0.5×0.5 mm ($L_e/t = 2$). Trend curves of the failure
 14 strain F_2 as a function of the natural logarithm of the strain rate are also presented in Fig. 8. Markers indicate
 15 the failing points calibrated by uniaxial tensile \circ , perforation \diamond and tearing Δ tests. The size of the markers
 16 are such that the larger ones denote higher strain rates.

17 When the calibration of the strain at failure is based on uniaxial tensile or perforation tests, a decrease around
 18 40% is observed in the plastic strain at rupture as the strain rate increases. In contrast to tensile and
 19 perforation tests, when the calibration of the strain at failure is based on the tearing tests, the plastic strain at
 20 failure increases up to 60% at high strain rates.

1 Figures 8b and 8c also present the F_2 curves of failure strain versus strain rate for element sizes of 2 and 5 mm
 2 ($L_{eq}/t = 8$ and 20 respectively) obtained by interpolation by weighting with f_1 . The interpolation curves agreed
 3 with the FE reproduction of perforation and tearing tests at different strain rates when using larger element
 4 sizes, 2 and 5 mm ($L_e/t = 8$ and 20 respectively).

5 Similarly to f_1 , normalized curves for F_2 are also formulated as f_2 considering a reference strain rate of $\dot{\epsilon}_0 =$
 6 0.2 s^{-1} in the form

7
$$f_2(\dot{\epsilon}) = F_2(\dot{\epsilon})/F_2(\dot{\epsilon}_0) \quad (14)$$



8
 9 Fig. 8. Strain rate sensitivity of failure strain considering a mesh size of $L_e = 0.5, 2$ and 5 mm (L_e/t ratios of 2,
 10 8 and 20).

11 3.7 Material failure models

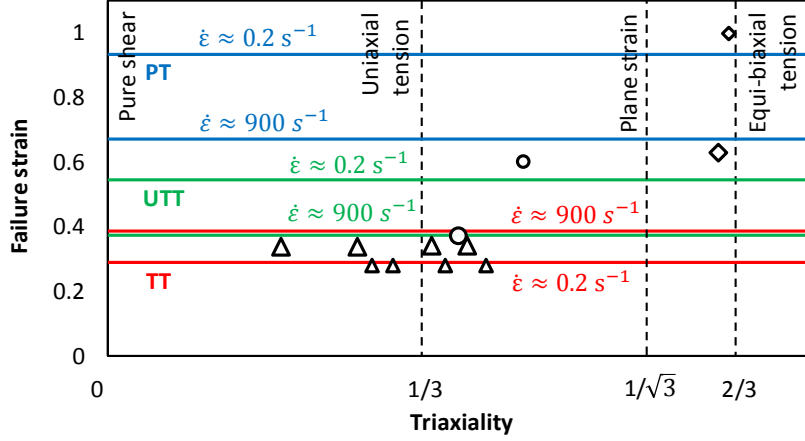
12 3.7.1 Plastic strain-based failure criterion

13 First, a simple plastic strain-based failure criterion (equivalent plastic strain at failure dependent on the mesh
 14 size and strain rate) is proposed for each one of the calibration mechanical tests (uniaxial tensile, perforation
 15 and tearing tests) as follows:

16
$$\varepsilon_f(L_e/t, \dot{\epsilon}) = f_1(L_e/t) f_2(\dot{\epsilon}) \varepsilon_{f_0} \quad (15)$$

17 where f_1 is the normalized failure strain as a function of the L_e/t ratio measured at a reference strain rate
 18 ($\dot{\epsilon}_0$), f_2 is the normalized failure strain as a function of the strain rate at a reference equivalent element length
 19 (L_{e_0}) and ε_{f_0} is the failure strain calibrated at a reference strain rate ($\dot{\epsilon}_0$) and a reference equivalent element
 20 length (L_{e_0}). An equivalent element length of $L_{e_0} = 0.5 \text{ mm}$, plate thickness $t = 0.25 \text{ mm}$ and a reference

1 strain rate around $\dot{\epsilon}_0 = 0.2 \text{ s}^{-1}$ were considered. Formulae $f_1(L_e/t)$, $f_2(\dot{\epsilon})$ and parameter $\epsilon_{f,0}$, for each one of
 2 the mechanical tests, are described in Appendix B. Figure 9 shows the failure locus for the plastic strain based
 3 on this failure criterion. The same failing points calibrated by uniaxial tensile, perforation and tearing tests,
 4 already presented in Fig. 6, are indicated by the markers \circ , \diamond and Δ , respectively, in Fig. 9.



5
 6 Fig. 9. Fracture locus for the plastic strain-based failure criterion in the triaxiality-failure strain space
 7 calibrated using uniaxial tensile tests (UTT), perforation tests (PT) and tearing tests (TT).

8 3.7.2 Stress state-based failure criterion

9 As observed previously in section 3.4, the stress states induced in the element just before its failure deletion
 10 are dependent on the type of mechanical test: uniaxial tensile, perforation or tearing.

11 The ductile fracture criterion proposed by Lou et al. (2012) was adopted in this work to include the triaxiality
 12 dependence on the material failure due to its simplicity and straightforward calibration. This criterion was
 13 constructed with consideration of damage accumulation induced by nucleation, growth and shear coalescence
 14 of voids (as stated by Lou et al., 2012). Despite its concept be grounded on solid elements, it was implemented
 15 for plane stress applications, i.e., shell elements. The failure criterion is given as follows:

$$16 \left(\frac{2 \tau_{max}}{\sigma_{eq}} \right)^{C_1} \left(\frac{(1+3\eta)}{2} \right)^{C_2} \epsilon_f = C_3 \quad (16)$$

17 or

$$18 \epsilon_f = C_3 \left(\frac{2 \tau_{max}}{\sigma_{eq}} \right)^{-C_1} \left(\frac{(1+3\eta)}{2} \right)^{-C_2} \quad (17)$$

$$19 \tau_{max} = \frac{1}{2} \max\{ |\sigma_1 - \sigma_2|, |\sigma_2 - \sigma_3|, |\sigma_3 - \sigma_1| \} \quad (18)$$

1 where $\langle x \rangle = x$ if $x > 0$ or $\langle x \rangle = 0$ if $x \leq 0$, τ_{max} is the maximum shear stress, σ_{eq} is the Von Mises stress,
 2 η is the stress triaxiality, ε_f is the failure strain and C_1 , C_2 and C_3 are material parameters.

3 In order to include the mesh size and strain rate sensitivity, this criterion was coupled with average normalized
 4 trend curves \bar{f}_1 and \bar{f}_2 by weighting the parameter C_3 as follows

$$5 \quad \varepsilon_f = \bar{f}_1(L_e/t) \bar{f}_2(\dot{\varepsilon}) C_3 \left(\frac{2 \tau_{max}}{\sigma_{eq}} \right)^{-C_1} \left(\frac{\langle 1+3\eta \rangle}{2} \right)^{-C_2} \quad (19)$$

6 The stress triaxialities – induced by the uniaxial tensile, perforation and tearing tests – cover uniformly the
 7 whole triaxiality range observed in failure occurrence of thin shell elements, i.e. from pure shear, uniaxial
 8 tension, plain strain to equi-biaxial tension, as shown in Fig. 6. So, the average normalized trend curves can be
 9 obtained by averaging the curves obtained from the three mechanical tests as follows:

$$10 \quad \bar{f}_1(L_e/t) = \frac{1}{3} \{f_1^{UTT} + f_1^{PT} + f_1^{TT}\}(L_e/t) \quad (20)$$

$$11 \quad \bar{f}_2(\dot{\varepsilon}) = \frac{1}{3} \{f_2^{UTT} + f_2^{PT} + f_2^{TT}\}(\dot{\varepsilon}) \quad (21)$$

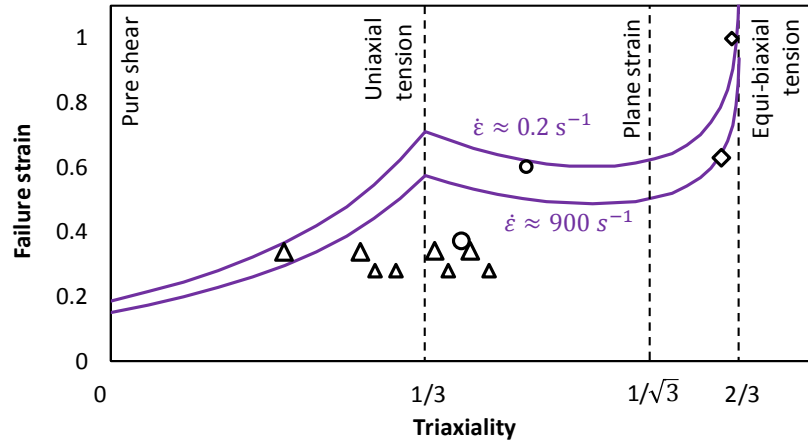
12 where UTT, PT and TT denote trend curves f_1 and f_2 obtained from uniaxial tensile tests, perforation tests and
 13 tearing tests respectively.

14 The material parameters $\{C_1, C_2, C_3\}$ are $\{3.5, -1.2, 0.71\}$. They were calibrated based on failure strains
 15 obtained from uniaxial tensile, perforation and tearing tests and considering an equivalent element length of
 16 $L_{e_0} = 0.5$ mm, plate thickness $t = 0.25$ mm ($L_{e_0}/t = 2$) and a reference strain rate around $\dot{\varepsilon}_0 = 0.2$ s⁻¹.

17 As a result, it can be observed in Fig. 10 that fitting the curve through all the points was not possible. While a
 18 good adjustment was obtained for perforation tests at low and high strain rates (0.2 and 900 s⁻¹ respectively),
 19 a good match was only achieved for uniaxial tensile test at low strain rate. Besides, it is very difficult to achieve
 20 a good correspondence with tearing tests points given their reverse behavior: higher strain rates lead to higher
 21 failure strains. However, a lower ceiling was considered for shear failure ($0 < \eta < 1/3$) irrespective of being at
 22 low or high strain rates.

23 This failure criterion was implemented in the commercial code Abaqus/CAE 2016 as “Ductile Damage” model
 24 by listing the fracture strain as a function of stress triaxiality and strain rate. No damage softening was
 25 considered by setting the parameter “displacement at failure” to zero.

1 The failure locus for the stress state based on this failure criterion is shown in Fig. 10. The same failing points
 2 calibrated by uniaxial tensile, perforation and tearing tests, already presented in Fig. 6, are indicated by the
 3 markers \circ , \diamond and Δ respectively in Fig. 10.



4
 5 Fig. 10. Fracture locus for the stress state-based failure criterion (SSBC) in the triaxiality-failure strain space.

6 **4. Case study: Miniature ship grounding test**

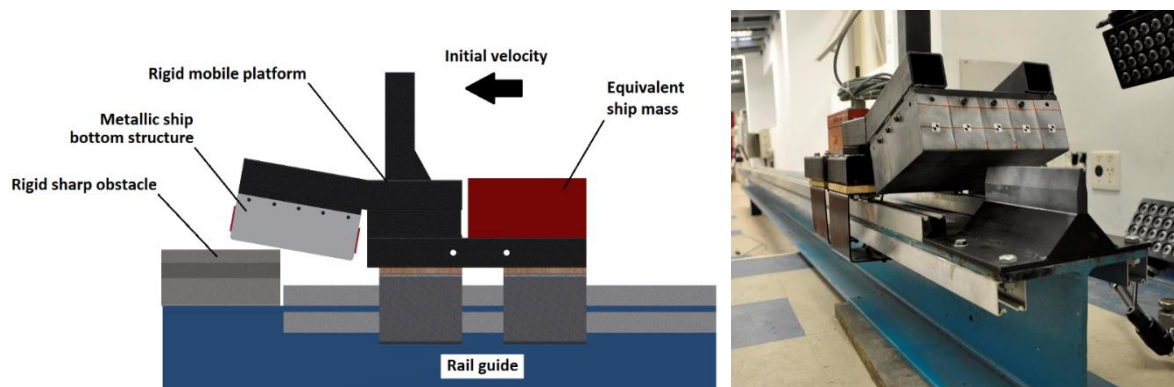
7 **4.1 Experiment**

8 A ship grounding accident was reproduced experimentally in a 1:100 reduced scale. A ship grounding scenario
 9 involves a combined vertical/horizontal movement of the ship bottom structure over a rigid sharp rock in the
 10 seabed.

11 A ship bottom structure of an oil tanker was manufactured in 0.01 scale reduction using the 0.25 mm thick
 12 mild steel sheets tested in the previous section. The ship bottom structure consists in a double plate panel
 13 structure of 210 × 230 × 23 mm with four horizontal and four vertical web frames uniformly distributed.
 14 Secondary stiffening structures and cutouts were disregarded. All parts were laser cut, mounted and laser
 15 welded.

16 The experimental arrangement consists in a ship bottom structure mounted in a horizontal slider colliding at
 17 2.47 m/s against a rigid sharp indenter at an angle of 19.8° (so inducing a relative vertical/horizontal
 18 penetration). The rest of the ship body was simplified as a mass in the mobile platform guided in the horizontal
 19 slider. This platform, mass and the ship bottom structure resulted in a total mass of 51.04 kg (Calle et al.,
 20 2017a).

1 The experimental measurement of the structure motion during the test time (about 0.1 s) was performed
 2 using a high-speed digital camera recording at 20,000 frames per second and a motion tracking software. From
 3 the high-speed camera images, the structure position, $x(t)$, is measured directly from the structure frame
 4 position, which is assumed to move as a rigid body. Next, the velocity and acceleration of the structure are
 5 obtained by the first and second time derivative of the position signal respectively, such as $\dot{x} = dx(t)/dt$ and
 6 $\ddot{x} = d^2x(t)/dt^2$. The horizontal force is finally evaluated by multiplying acceleration by the total platform
 7 mass (M) in the form: $F(t) = M \ddot{x}(t)$.



8
 9 Fig. 11. Scheme and experimental setup of ship grounding test in miniature.

10 As a result, the outer plate of the ship bottom structure was torn locally by the frontal face of the rigid obstacle
 11 so causing a predominant global tearing collapse of the structure as shown in Fig. 12. The plate cut off by the
 12 obstacle was folded and pressed against the last transversal plate. The area of the torn plate increased
 13 progressively after the second transversal web frame, Fig. 12, but it was continually delimited by the horizontal
 14 web frames. The internal transversal web frames showed a structural collapse partially stretched before being
 15 torn by the rigid obstacle, Fig. 13.
 16 Occurrence of rupture in welded joints was not significant in the structural collapse as a whole, barely the joint
 17 between the transversal reinforcement and the inner plate showed complete weld fillet detachment, Fig. 12.



1

2

Fig. 12. Collapsed ship bottom structure: overall collapse with obstacle and torn outer plate.

3

The resulting reaction force (in the horizontal direction) from the ship grounding experiment is directly related

4

with the inner collapse of the double plate bottom structure as shown in Fig. 13. The initial contact between

5

the rigid obstacle and the miniature ship bottom structure occurs in point ① at zero force, the outer plate is

6

stretched up to a maximum peak force ② just before outer plate perforation (Similarly, a small peak force is

7

detected when perforates the inner plate in ⑤). The reaction force remains close to steady during the outer

8

plate tearing process: ② to ⑤). Small force peaks are observed when the rigid obstacle contacts each one of

9

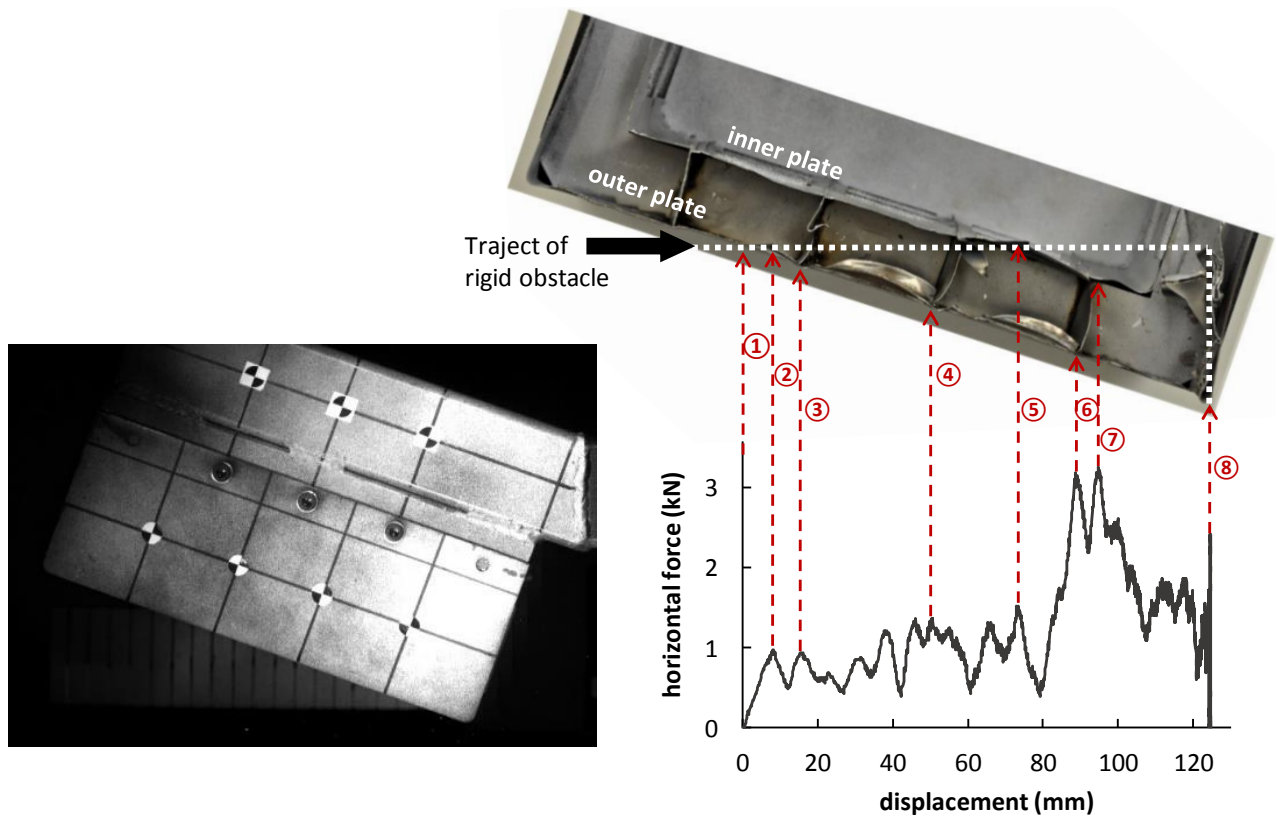
the structural joints in outer plate, ③ and ④, and large force peaks in both outer and inner plates, ⑥ and

10

⑦). Finally, the maximum displacement of the structure is achieved in ⑧ when all the kinetic energy is

11

consumed and the reaction force falls to zero.



1

2

Fig. 13. Experimental reaction force and correlation with internal structure collapse.

3

4.2 FE modeling

4

A finite element model of the ship bottom structure was created in the commercial code Abaqus/CAE 2016

5

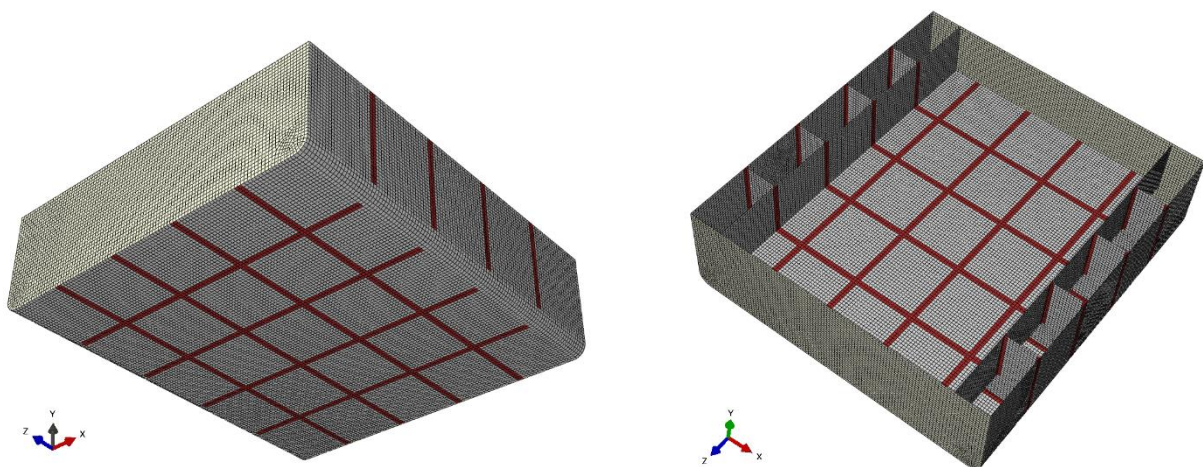
considering the mid-plane dimensions of the structure and 2×2 mm shell elements for both mild steel and

6

welded joints as shown in Fig. 14. The indenter and the mobile base for the ship bottom structure were

7

modeled as rigid bodies and a general friction coefficient of 0.1 was considered between all contact surfaces.



8

9

Fig. 14. Mesh of ship bottom structure: outer plate and inner plate views.

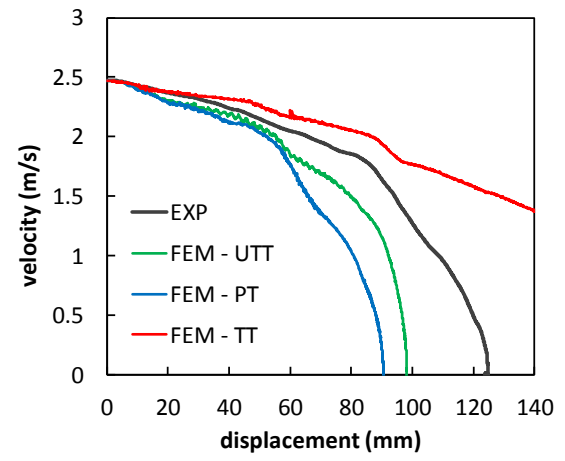
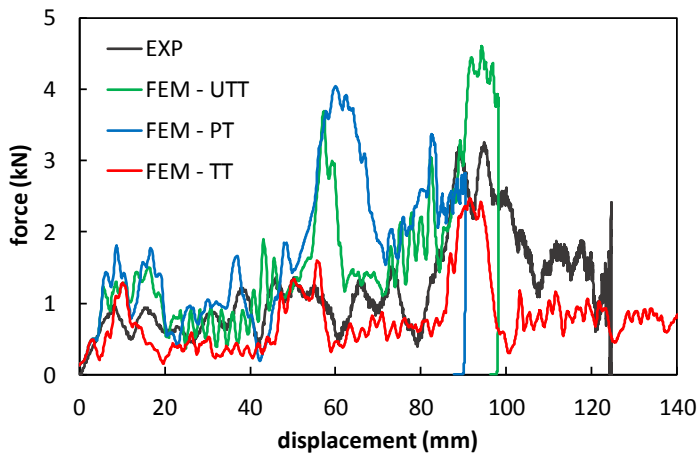
1 The elasto-plastic behavior of the base material (0.25 mm thick mild steel sheet) was modeled using the
2 coupled Power law plus Alves model seen previously in section 2. The laser-welded joints were modeled using
3 the same elasto-plastic behavior of the base material, but considering a failure strain of 0.2064 calibrated
4 using tensile test experiments in welded strip samples and considering plastic work equivalence (similar to the
5 procedure for failure in tensile test calibration, section 3.1).

6 The performance of the plastic strain-based failure criteria with strain rate and mesh size sensitivity (shown in
7 Fig. 9) for the base material is evaluated. These criteria calibrated from tensile, perforation and tearing tests
8 are named as UTT, PT and TT criteria respectively. The experimental response is here called as EXP.

9 Figure 15 also presents the force-displacement responses generated numerically by employing the UTT, PT
10 and TT failure criteria with strain rate sensitivity shown in Fig. 9. However, none of those generated compatible
11 results with that obtained in the experiment. Among these criteria, TT failure criterion produced force levels
12 closer to that obtained experimentally, probably because the plate tearing (crack propagation) is dominant in
13 the overall structure collapse as seen in Fig. 15.

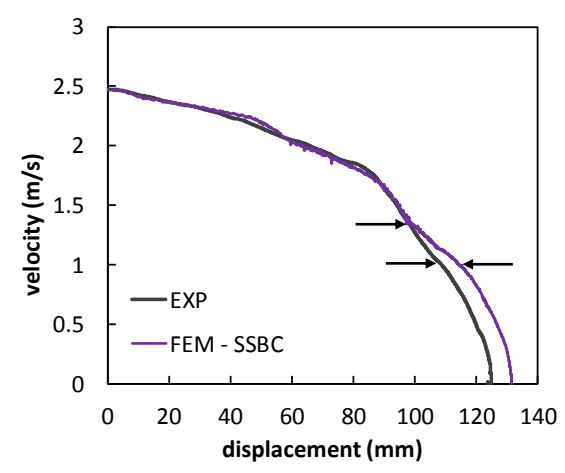
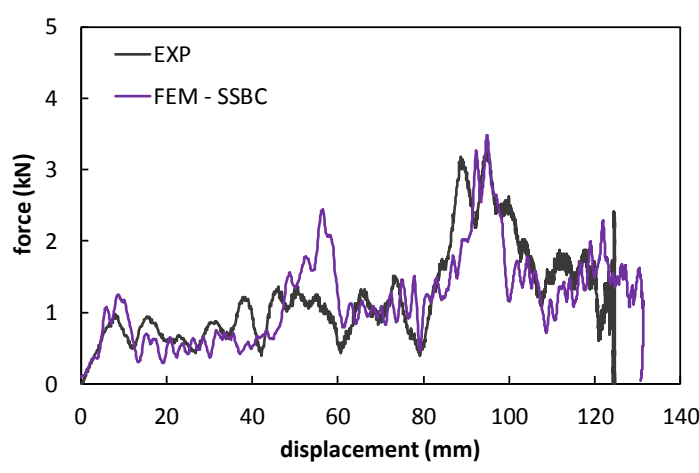
14 The performance of the stress state-based failure criterion (SSBC) coupled with strain rate and mesh size
15 sensitivities, Eq. (19), showed to be superior to that obtained by all the plastic strain-based failure criteria,
16 regardless of the type of mechanical test.

17 When analyzing the kinematic response, a slight difference between the experimental and numerical velocity
18 histories is observed from 100 to 110 mm displacement as pointed with arrows in Fig. 16. This divergence was
19 mainly generated by the inaccurate modeling of the accumulated folded material that, in turn, generated a
20 slight crack propagation deviation in the ship bottom structure. Consequently, the modeled crack path
21 demanded less energy for penetration so inducing an increase in the final obstacle penetration of about +4.7%.



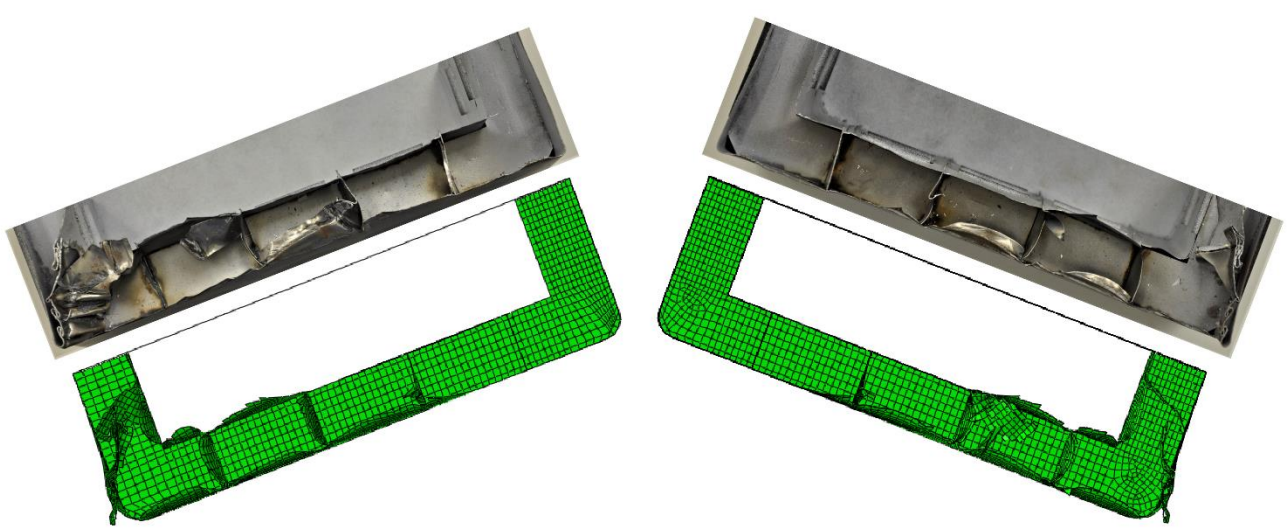
1
2

Fig. 15. Force and velocity responses obtained numerically using UTT, PT and TT failure criteria.



3
4

Fig. 16. Force and velocity responses obtained numerically using the stress state-based criterion (SSBC).



5
6

Fig. 17. Sectioned views of collapsed ship bottom structure: right and left sections.

1 4.3 Strain rate

2 For marine structures subjected to collision and grounding, certain areas of their structural members can
3 undergo plastic deformation at high strain rates, but not necessarily all these areas can lead to material
4 fracture. For instance, the local buckling of a structural member can generate large localized plastic
5 deformation in the hinge area but not always leading to material rupture.

6 However, it is very common to observe material rupture in intersection joints of marine structures subjected
7 to collision because of the high stress concentration. Storheim and Amdahl (2017) evaluated numerically the
8 crushing of a bulb tip, so resulting in a strain rates associated with plastic strain between 5 and 15 s⁻¹. They
9 also stated that strain rates can achieve values up to 100 s⁻¹ in ship collision simulations considering shell
10 elements with L_e/t ratios between 5 and 10. However, they did not specify if the elements that undergo high
11 strain rates achieve rupture.

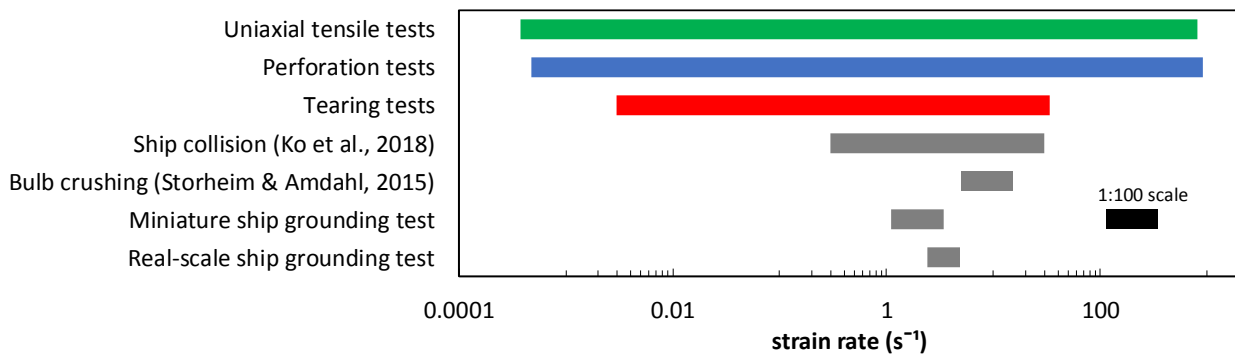
12 Furthermore, Ko et al. (2018) performed FE modeling of the lateral ship collision with varying collision speeds
13 (from 0.5 to 20 knots) so resulting in the rupture of the side shell of the struck ship at strain rates from 0.3 to
14 30 s⁻¹. L_e/t ratios around 5 were considered in the fine mesh of structural members near the collision location.
15 Here, in the numerical modeling of the miniature ship grounding test with uniform shell elements with a L_e/t
16 ratio of 8, strain rates in the range of 110-340 s⁻¹ are observed in failing elements subjected mainly to tearing
17 and stretching. When bringing this miniature experiment to real scale using similarity laws (scaling formulae
18 detailed by Oshiro and Alves, 2009; Oshiro et al., 2017), this strain rate range corresponds to 1.1-3.4 s⁻¹. This
19 range is compatible with that obtained from FE modeling of the grounding experiment but in real scale, which
20 generates strain rates in failing elements in the range of 2.4 to 4.9 s⁻¹.

21 All these strain rate ranges resulting from ship collision events are compared in Fig. 18. The strain rate range
22 obtained from the miniature ship grounding test showed to be compatible with that obtained from real-scale
23 ship collision studies.

24 The high levels of strain rates induced in the miniature ship grounding experiment, when compared against
25 the strain rate levels induced in real scale events, ended up intensifying the influence of the strain rate

1 sensitivity on the failure criterion and, consequently, on the structural response. So, as lower strain rates are
 2 expected in real scale tests, lower influence of the strain rate sensitivity is also expected.

3 The strain rate ranges comprised by the tensile, perforation and tearing tests at different test velocities are
 4 also included in Fig. 18. The strain rates obtained by the mechanical tests cover, almost completely, the strain
 5 rate ranges observed in miniature and real scale ship collision/grounding events.



6
 7 Fig. 18. Strain rates ranges obtained from mechanical tests and FE simulations of ship collision/grounding.

8 5. Conclusions

9 In this work the effect of the strain rate on the failure strain and the type of mechanical test used for the
 10 failure calibration are evaluated experimentally and numerically. Then, a miniature ship grounding experiment
 11 was FE modeled to corroborate the real influence of these aspects when modeling collision events. A double-
 12 plate bottom structure of a tanker ship, in 1:100 reduction scale, was considered for the experiment. This
 13 structure was made of a 0.25 mm thickness mild steel plate, cut and welded by laser.

14 The effect of the strain rate on the material fracture of mild steel plates when subjected to different
 15 mechanical tests was evaluated by uniaxial tensile, perforation and tearing experiments at different loading
 16 rates. The aim of these singular mechanical tests is to cover, to the extent possible, the fracture modes
 17 observed in marine structures subjected to collision/grounding related to crack initiation and propagation.

18 In general, experiments related to crack initiation (uniaxial tensile and perforation tests) showed failure strains
 19 substantially higher than that related to crack propagation (tearing tests). Uniaxial tensile and perforation
 20 tests presented a decrease in the failure strains at high strain rates while tearing tests presented an opposite
 21 effect, i.e., failure strains' increase together with strain rates. Yet all tests presented a decrease in the failure
 22 strains with the increase of the element mesh size.

1 Different to that observed in uniaxial tensile and perforation tests ($0.33 < \eta < 0.66$), tearing tests induced
2 strong oscillations in the stress triaxiality in failing elements before fracture occurrence. In spite of these
3 oscillations, it can be stated that the stress state induced in tearing tests is located more heavily between pure
4 shear and uniaxial tensile regimes ($0.0 < \eta < 0.33$).

5 The collapse mode observed in the miniature ship bottom structure, generated in the ship grounding
6 experiment, is an alternating combination of stretched and torn structural members along the penetration
7 path, so exhibiting clearly material rupture governed by both crack initiation and propagation.

8 Two failure criteria were employed to FE model the miniature ship grounding experiment: a plastic strain-
9 based criterion and a stress state-based criterion, both involving sensitivity to element size and strain rate.

10 The plastic strain-based failure criterion failed in reproducing accurately the structural response and collapsed
11 mode obtained from the miniature ship grounding experiment. When the failure criterion is calibrated based
12 on mechanical tests related to crack initiation (uniaxial tensile or perforation tests), it tends to overestimate
13 the demanded energy for material fracture, while, when calibration is based on crack propagation (tearing
14 tests), it tends to underestimate this energy.

15 In addition, the stress state-based failure criterion successfully managed to include all these effects through
16 stress triaxiality dependence so resulting in a more accurate structural response and collapse mode. To extend
17 effectively this criterion to shipbuilding steels, new tests would be required focusing specifically these
18 materials.

19 **6. Acknowledgements**

20 The authors would like to thank Sao Paulo State Research Foundation (FAPESP 2011/11733-3), the National
21 Council for Scientific and Technological Development (CNPq 501978/2014-3) and Brazilian Research Funding
22 Agency (FINEP 01.10.0511.00) for the financial support to this work.

23 **7. Data availability**

24 The raw experimental data from all tensile, perforation and tearing tests presented in this work are available
25 to download from <http://dx.doi.org/10.17632/8k43xh5fv8.2>.

26 **8. References**

1 AbuBakar, A., Dow, R.S., Simulation of ship grounding damage using the finite element method,
2 International Journal of Solids and Structures, Vol. 50(5), pp. 623-636, 2013.

3 Alsos, H. S. and Amdahl, J., 'On the resistance of tanker bottom structure during stranding', Marine
4 Structures, Vol. 20, n. 4, pp. 2018-237, 2007.

5 Alves, M., Material Constitutive Law for Large Strains and Strain Rates, Journal of Engineering
6 Mechanics, 2000, Vol. 126, n. 2, pp. 215-218, 2000.

7 Bela, A., Le Sourne, H., Buldgen, L., Rigo, P., Ship collision analysis on offshore wind turbine monopile
8 foundations, Marine Structures, Vol. 51, pp. 220-241, 2017.

9 Calle, M. A. G. and Alves, M., 'A review-analysis on material failure modeling in ship collision', Ocean
10 Engineering, Vol. 106, pp. 20-38, 2015.

11 Calle, M.A.G., Oshiro, R.E., Alves, M., Ship collision and grounding: Scaled experiments and numerical
12 analysis, International Journal of Impact Engineering, Vol. 103, pp. 195-210, 2017a.

13 Calle, M.A.G., Verleysen, P., Alves, M., Benchmark study of failure criteria for ship collision modeling
14 using purpose-designed tensile specimen geometries, Marine Structures, Vol. 53, pp. 68-85, 2017b.

15 Choung, J., Cho, S-R., Kim, K.S., Impact test simulations of stiffened plates using the micromechanical
16 porous plasticity model, Ocean Engineering, Vol. 37, n. 8-9, pp. 749-756, 2010.

17 Choung, J., Shim, C-S., Song, H-C., Estimation of failure strain of EH36 high strength marine structural
18 steel using average stress triaxiality, Marine Structures, Vol. 29, pp. 1-21, 2012.

19 Choung, J., Nam, W., Lee, J-Y., Dynamic hardening behaviors of various marine structural steels
20 considering dependencies on strain rate and temperature, Marine Structures, Vol. 32, pp. 49-67, 2013.

21 Cowper, G.R., Symonds, P.S., Strain-hardening and strain-rate effects in the impact loading of
22 cantilever beams, Technical report n. 28. Providence, USA: Division of Applied Mathematics, Brown University,
23 1957.

24 Ehlers S, Varsta P., Strain and stress relation for non-linear finite element simulations, Thin-Walled
25 Structures, Vol. 47, pp. 1203-1217, 2009.

1 Ehlert S., Strain and stress relation until fracture for finite element simulations of a thin circular plate,
2 Thin-Walled Structures, Vol. 48(1), pp. 1–8, 2010.

3 Endo, H., Yamada, Y., Kitamura, O., Suzuki, K., Model test on the collapse strength of the buffer bow
4 structures, Marine Structures, Vol. 15 (4–5), pp. 365-381, 2002.

5 Farinha, A., Sousa, L., Reis, L., Evaluating lock gates' strength due to ship collisions: A Douro waterway
6 lock gates case study, Marine Structures, Vol. 60, pp. 261-278, 2018.

7 Flores, F.G., A simple reduced integration hexahedral solid-shell element for large strains, Computer
8 Methods in Applied Mechanics and Engineering, Vol. 303, pp. 260-287, 2016.

9 Hogström, P., RoPax ship collision - A methodology for survivability analysis, Department of Shipping
10 and Marine Technology, Chalmers University of Technology, p. 84, Ph.D. Thesis, 2012.

11 Johnson, G., Cook, W., Fracture characteristics of three metals subjected to various strains, strain
12 rates, temperatures and pressures, Engineering Fracture Mechanics, Vol. 21, pp. 31-48, 1985.

13 Jones, N., 'On the dynamic inelastic failure of beams', In: Structural Failure, Ed. Wiley, New York, USA,
14 pp. 133-159, 1989.

15 Kapoor, R., Nemat-Nasser, S., Determination of temperature rise during high strain rate deformation,
16 Mechanics of Materials, Vol. 27, n. 1, pp. 1-12, 1998.

17 Kim, K.J., Lee, J.H., Park, D.K., Jung, B.G., Han, X., Paik, J.K., An experimental and numerical study on
18 nonlinear impact responses of steel-plated structures in an Arctic environment, International Journal of Impact
19 Engineering, Vol. 93, pp. 99-115, 2016.

20 Kitamura, O., Endo, H., Collision simulations of an exclusive ship of spent nuclear fuels. In: Proceedings
21 of the International Workshop on Utilization of Nuclear Power in Oceans, N'Ocean 2000, Tokyo, Japan, 2000.

22 Körgesaar, M., Romanoff, J., 'Influence of softening on fracture propagation in large-scale shell
23 structures', International Journal of Solid and Structures, v. 50, pp. 3911-3921, 2013.

24 Körgesaar, M., Romanoff, J., Influence of mesh size, stress triaxiality and damage induced softening
25 on ductile fracture of large-scale shell structures. Marine Structures, Vol. 38, pp. 1–17, 2014.

1 Körgesaar, M., The effect of low stress triaxialities and deformation paths on ductile fracture
2 simulations of large shell structures, *Marine Structures*, Vol. 63, pp. 45-64, 2019.

3 Ko, Y.G., kim S.J., Sohn, J.M., Paik, J.K., A practical method to determine the dynamic fracture strain
4 for the nonlinear finite element analysis of structural crashworthiness in ship-ship collisions, *Ship and Offshore
5 Structures*, Vol. 13(4), pp. 412-422, 2018.

6 Lee, Y-W., Woertz, J.C., Wierzbicki, T., Fracture prediction of thin plates under hemi-spherical punch
7 with calibration and experimental verification, *International Journal of Mechanical Sciences*, Vol. 46(5), pp.
8 751-781, 2004.

9 Lehmann, E., Yu, X., On ductile rupture criteria for structural tear in the case of ship collision and
10 grounding, *Practical Design of Ships and Mobile Units*, Elsevier Science, B.V., 1998.

11 Liu, B., Pedersen, P.T., Zhua, L., Zhang, S., Review of experiments and calculation procedures for ship
12 collision and grounding damage, *Marine Structures*, Vol. 59, pp. 105–121, 2018.

13 Lou, Y., Huh, H., Lim, S., Pack, K., New ductile fracture criterion for prediction of fracture forming limit
14 diagrams of sheet metals, *International Journal of Solids and Structures*, Vol. 49(25), pp. 3605-3615, 2012.

15 Marinatos, J.N., Samuelides, M.S., Towards a unified methodology for the simulation of rupture in
16 collision and grounding of ships, *Marine Structures*, Vol. 42, pp. 1-32, 2015.

17 Mason, J. J., Rosakis, A. J., Ravichandran, G., On the strain and strain rate dependence of the fraction
18 of plastic work converted to heat: an experimental study using high speed infrared detectors and the Kolsky
19 bar, *Mechanics of Materials*, Vol. 17, n. 2–3, pp. 135-145, 1994.

20 Nguyen, T-H., Amdahl, J., Leira, B.J., Garrè, L., Understanding ship-grounding events, *Marine
21 Structures*, Vol. 24, n. 4, pp. 551-569, 2011.

22 Nguyen, T-H., Garrè, L., Amdahl, J., Leira, B.J., Benchmark study on the assessment of ship damage
23 conditions during stranding, *Ships and Offshore Structures*, Vol. 7, n. 2, pp. 197–213, 2012.

24 Oshiro, R.E., Alves, M., Scaling of structures subject to impact loads when using a power law
25 constitutive equation, *International Journal of Solids and Structures*, Vol. 46, pp. 3412-3421, 2009

1 Oshiro, R.E., Calle, M.A.G., Mazzariol, L.M., Alves, M., Experimental study of collision in scaled naval
2 structures, *International Journal of Impact Engineering*, Vol. 110, pp. 149-161, 2017.

3 Paik, J.K., Practical techniques for finite element modeling to simulate structural crashworthiness in
4 ship collisions and grounding (Part I: Theory), *Ships and Offshore Structures*, v. 2, n. 1, pp. 69-80, 2007a.

5 Paik, J.K., Practical techniques for finite element modelling to simulate structural crashworthiness in
6 ship collisions and grounding (Part II: Verification), *Ships and Offshore Structures*, v. 2, n. 1, pp. 81-85, 2007b.

7 Paik, J.K. and Pedersen, P.T., 'Modelling of the internal mechanics in ship collisions', *Ocean*
8 *Engineering*, v. 23, n. 2, pp. 107-142, 1996.

9 Paik, J.K. and Thayamballi, A.K., 'Ultimate limit state design of steel-plated structures', Ed. Wiley,
10 Chichester, United Kingdom, 544 p., 2003.

11 Paik, J.K., Kim, K.J., Lee, J.H., Jung, B.G. and Kim, S.J., Test database of the mechanical properties of
12 mild, high-tensile and stainless steel and aluminium alloy associated with cold temperatures and strain rates,
13 *Ships and Offshore Structures*, Vol. 12(S1), pp. S230-S256, 2017.

14 Peschmann, J., Kulzep, A., Side collision of double skin ships, Final report for BMBF Life-cycle design,
15 Technical University of Hamburg, 2000.

16 Roth, C.C., Mohr, D., Effect of strain rate on ductile fracture initiation in advanced high strength steel
17 sheets: Experiments and modeling, *International Journal of Plasticity*, Vol. 56, pp. 19-44, 2014.

18 Simonsen, B.C. and Törnqvist, R., 'Experimental and numerical modelling of ductile crack propagation
19 in large-scale shell structures', *Marine Structures*, v. 17, pp. 1-27, 2004.

20 Storheim, M., Amdahl, J., On the sensitivity to work hardening and strain-rate effects in nonlinear FEM
21 analysis of ship collisions, *Ship and Offshore Structures*, Vol. 12, n. 1, pp. 1-16, 2017.

22 Storheim, M., Amdahl, J., Martens, I., On the accuracy of fracture estimation in collision analysis of
23 ship and offshore structures, *Marine Structures*, Vol. 44, pp. 254-287, 2015.

24 Soares and Garbatov, Editors of Proceedings of the 19th International Ship and Offshore Structures
25 Congress Vol. 2, Report V.2, p. 605, Cascais, Portugal, 2015.

1 Törnqvist, R., Design of crashworthy ship structures, Technical University of Denmark, p. 243, Ph.D.
2 Thesis, 2003.

3 Verleysen, P., Degrieck, J., Verstraete, T., Van Slycken, J., Influence of specimen geometry on split
4 Hopkinson tensile bar tests on sheet materials, Experimental Mechanics, Vol. 48, pp. 587-598, 2008.

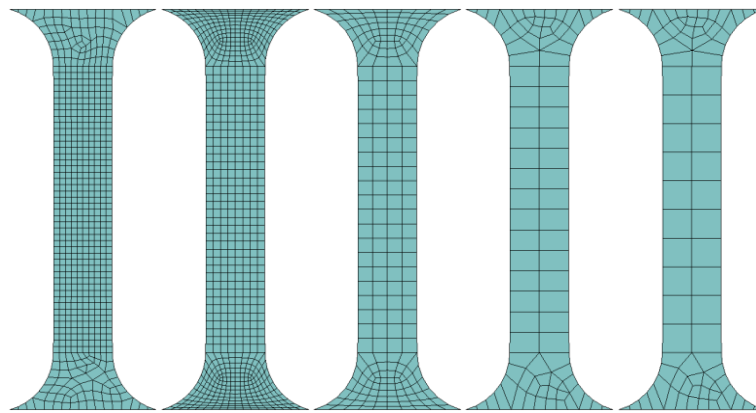
5 Wiśniewski, K., Kołakowski, P., The effect of selected parameters on ship collision results by dynamic
6 FE simulations, Finite Element in Analysis and Design, vol. 39, pp. 985–1006, 2003.

7 Yagi, S., Kumamoto, H., Muragishi, O., Takaoka, Y., Shimoda, T., A study on collision buffer
8 characteristic of sharp entrance angle bow structure, Marine Structures, Vol. 22 (1), pp. 12-23, 2009.

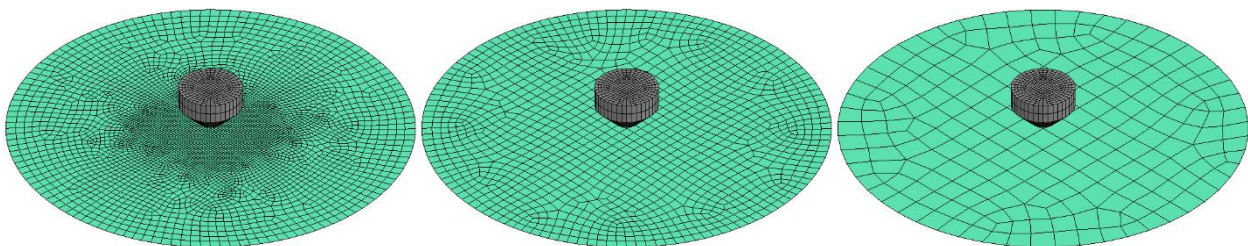
9 Yamada, Y., Endo, H. and Pedersen, P.T., 'Numerical study on the effect on buffer bow structure in
10 ship-ship collision', 15th International Offshore and Polar Engineering Conference, Seoul, Korea, pp. 604-611,
11 2005.

12 **Appendixes**

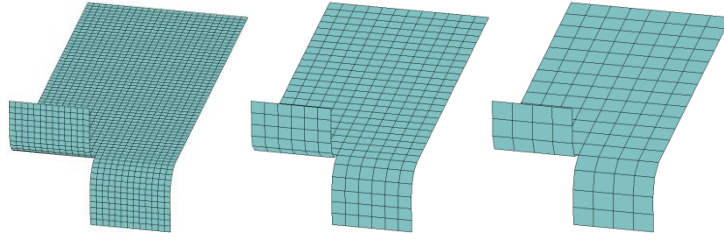
13 Appendix A. Mesh configurations for tensile, perforation and tearing tests using different mesh sizes



14
15 A1. Mesh models for tensile test with $L_e/t = 4, 6.67, 10, 16.33$ and 20.



16
17 A2. Mesh models for perforation tests with $L_e/t = 2, 8$ and 20.



A3. Mesh models for tearing tests with $L_e/t = 4, 7.3$ and 11.18 .

- 1
- 2
- 3 Appendix B. Trend curves for equivalent plastic strain at failure for tensile, perforation and tearing tests
- 4 dependent on mesh size and strain rate

Tensile tests	$F_1^{UTT}(L_e/t) = -0.00924 \cdot L_e/t + 0.6175$ obtained at quasi-static conditions (crosshead velocity of $v_0 = 0.0025$ mm/s) $F_1^{UTT}(L_{e_0}/t = 2.0) = 0.5990$ $f_1^{UTT}(L_e/t) = -0.015426 \cdot L_e/t + 1.03087$ $F_2^{UTT}(\dot{\epsilon}) = -0.02044942 \cdot \ln(\dot{\epsilon}) + 0.51242252$ obtained at a reference element length of $L_{e_0} = 0.5$ ($L_{e_0}/t = 2.0$) $F_2^{UTT}(\dot{\epsilon}_0 = 0.2 \text{ s}^{-1}) = 0.545335$ $f_2^{UTT}(\dot{\epsilon}) = -0.0375 \cdot \ln(\dot{\epsilon}) + 0.93965$ $\epsilon_{f0}^{UTT} = 0.545335$
Perforation tests	$F_1^{PT}(L_e/t) = 0.962022 \cdot e^{-0.06265 \cdot L_e/t}$ obtained at quasi-static conditions (indenter velocity of $v_0 = 0.0025$ mm/s) $F_1^{PT}(L_{e_0}/t = 2.0) = 0.8487$ $f_1^{PT} = 1.13348 \cdot e^{-0.06265 \cdot L_e/t}$ $F_2^{PT}(\dot{\epsilon}) = -0.03121 \cdot \ln(\dot{\epsilon}) + 0.88224$ obtained at a reference element length of $L_{e_0} = 0.5$ ($L_{e_0}/t = 2.0$) $F_2^{PT}(\dot{\epsilon}_0 = 0.2 \text{ s}^{-1}) = 0.93247$ $f_2^{PT}(\dot{\epsilon}) = -0.03347 \cdot \ln(\dot{\epsilon}) + 0.94613$ $\epsilon_{f0}^{PT} = 0.93247$

<p>Tearing tests</p>	<p>$F_1^{TT}(L_e/t) = 0.44947317(L_e/t)^{-0.67538904}$ obtained at quasi-static conditions (crosshead velocity of $v_0 = 0.01$ mm/s)</p> <p>$F_1^{TT}(L_{e_0}/t = 2.0) = 0.5764$</p> <p>$f_1^{TT}(L_e/t) = 0.7798(L_e/t)^{-0.67538904}$</p> <p>$F_2^{TT}(\dot{\epsilon}) = 0.01151233 \cdot \ln(\dot{\epsilon}) + 0.30599155$ obtained at a reference element length of $L_{e_0} = 0.5$ ($L_{e_0}/t = 2.0$)</p> <p>$F_2^{TT}(\dot{\epsilon}_0 = 0.2 \text{ s}^{-1}) = 0.28746$</p> <p>$f_2^{TT}(\dot{\epsilon}) = 0.04005 \cdot \ln(\dot{\epsilon}) + 1.064455$</p> <p>$\epsilon_{f0}^{TT} = 0.28746$</p>
<p>Average trend curves</p>	<p>$\bar{f}_1(L_e/t) = -0.12120804 \cdot \ln(L_e/t) + 0.66460069$</p> <p>$\bar{f}_2(\dot{\epsilon}) = -0.01338240 \cdot \ln(\dot{\epsilon}) + 0.56688443$</p>